Propagation and detection of RF-modulated electron and X-ray beams in air

J. R. Harris, C. N. Harris, R. B. Miller, and N. T. Myers

Citation: Journal of Applied Physics **123**, 223303 (2018); doi: 10.1063/1.5029938
View online: https://doi.org/10.1063/1.5029938
View Table of Contents: http://aip.scitation.org/toc/jap/123/22
Published by the American Institute of Physics

Propagation and detection of RF-modulated electron and X-ray beams in air

J. R. Harris,[1] C. N. Harris,[1] R. B. Miller,[2] and N. T. Myers[3]
[1]*Directed Energy Directorate, Air Force Research Laboratory, Albuquerque, New Mexico 87106, USA*
[2]*EBM, LLC, Albuquerque, New Mexico 87110, USA*
[3]*Verus Research, Albuquerque, New Mexico 87110, USA*

(Received 16 March 2018; accepted 26 May 2018; published online 12 June 2018)

Electron beams produced in RF linear accelerators will naturally be modulated at the RF frequency. Here we report measurements of the RF harmonic content of a 21.6 MeV electron beam coasting in air, as well as the RF harmonic content of x-rays produced from that electron beam, and the effects of these modulated electron and x-ray beams on several fast detection systems. The RF fundamental and its higher harmonics were found to be impressed onto the x-rays generated from the electron beam, and the response of an RF waveguide to passage of the modulated x-ray signal indicated that this harmonic content was also impressed onto the secondary electrons produced by the passage of the x-rays through the waveguide. An unexpected, interference-like effect was observed, which was particularly prominent in the case of the waveguide when struck by the modulated x-rays. The participation of secondary electrons produced by passage of the x-rays through the x-ray converter upstream of the waveguide was ruled out as a significant contributor to this effect. https://doi.org/10.1063/1.5029938

I. INTRODUCTION

The generation and use of modulated electron beams is at the heart of much of the technology and many applications of particle accelerators and vacuum electronics. All beams are modulated to some degree, and strong modulation can occur through a number of means including gating of the beam source[1–6] or through interaction with fields in RF linacs. Even when propagating in vacuum, where the most research has been done,[7–10] changes in beam modulation can occur through space charge wave evolution;[1,11,12] passage through apertures;[13,14] interactions with slow wave,[15] resistive,[7] or magnetic structures;[16] and nonlinear processes.[17,18] The beam's transverse and longitudinal dynamics will also be coupled through the presence of space charge in the beam.[7,19–21] Propagation of such modulated electron beams through air is also possible, although this introduces other interactions, such as scattering, plasma processes, and secondary radiation generation.[8] When modulated electron beams are used to generate x-rays, these x-rays may retain some of the original electron beam's modulation,[22] and both modulated electron and x-ray beams can interact with fast electronic and RF devices which can be used to detect that modulation.[23] Modulated x-ray beams, in particular, are of increasing interest for spacecraft communication[24–28] and range-finding[29] applications.

In a previous set of experiments,[22] we studied the transport of RF-modulated electron beams through air and metal, with a focus on understanding their subsequent interactions with RF cavities and waveguides. These results suggested that the electron beam's RF modulation was preserved, at least to some degree, even as the beam traveled through air and significant thicknesses of metal. They also suggested that this modulation was impressed not only onto the x-rays generated by those electron beams but also onto the secondary electrons generated as those x-rays passed through metal cavities and waveguides. To verify this, we sought (1) to directly measure the RF frequency content of an electron beam produced in an RF linac as it coasts in air, (2) to directly measure the RF frequency content of the x-rays produced from this modulated electron beam, and (3) to measure the RF frequency content of the signals these electrons and x-rays generate when interacting with RF structures. This was accomplished using the 25 MeV S-band electron linac at the Idaho Accelerator Center (IAC).[30] The accelerator's 2856 MHz RF frequency and its harmonics were detected in the electron beam and in the x-rays produced from it using (1) an unbiased diamond radiation measurement diode, (2) an S-band waveguide, (3) an S-band pillbox cavity, and (4) a $\dot{B}$ loop. These measurements verified that the RF fundamental and higher harmonics are retained in the x-ray beams produced when the primary electrons strike metal objects, and are still retained in the secondary electrons produced when the x-ray beam strikes metal objects. A surprising result from this testing was the observation of well-defined nulls in the induced signals in these RF devices as their distances downstream were changed. These nulls were most pronounced with RF-modulated x-ray beams and with larger-area targets and suggest the presence of an unexpected interference process occurring due to interaction of microwave signals generated at different locations and with different phase delays in the RF structure.

Our results will be discussed in detail in this article. Section II will describe our experimental apparatus and measurement techniques. Our primary experimental results will be grouped into three sections, with Sec. III covering electron beam transport in air, Sec. IV covering transport in air of RF-modulated x-rays, and Sec. V briefly describing tests with the electron beam striking Al plates. Section VI will detail measurements made to assess the role of secondary electrons in the generation of the interference-like nulls, and our results will be summarized in Sec. VII.

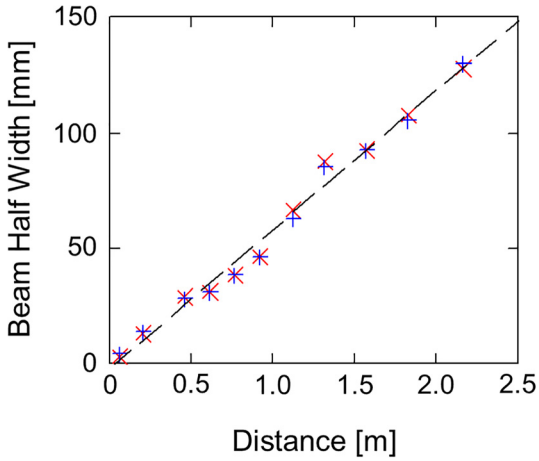

FIG. 1. Electron beam envelope. Vertical (blue +) and horizontal (red x) half widths as a function of distance, compared to linear fit with intercept of −2 mm and slope of 60×10^{-3}.

II. EXPERIMENTAL APPARATUS

The experiments reported here were performed using the electron beam generated with the 25 MeV S-band RF linac at IAC. This machine, a Varian Clinac, exhibits very stable and repeatable operation and was therefore ideal for this work. The machine was operated at a beam energy of 21.6 MeV, a nominal beam current of 95 mA, and a macropulse length of 4 μs, with the beam extracted through a 1 mil Ti foil beam window on the machine's zero degree port. The electron beam envelope in air was measured by placing glass plates at various distances downstream from the beam window, and using the resulting discoloration in the glass to indicate the beam size. The results of this measurement are shown in Fig. 1. The beam envelope was symmetrical in the horizontal and vertical directions and approximately linear with distance, with the beam's half-width described well by

$$w(z) = -0.002 + 0.06z\,[\mathrm{m}]. \quad (1)$$

Generation of x-rays could be accomplished using an x-ray converter consisting of a 0.254 cm W foil mounted on a water-cooled 2.29 cm Al block (Fig. 2). Some testing also used thin Al plates placed immediately downstream of the beam window.

To detect modulation in the electron and x-ray signals, we used several techniques (Fig. 2). The first was a diamond diode designed for radiation measurements and manufactured by Alameda Applied Science Corporation.[31] In normal operation, they are biased to 150 V and connected to an oscilloscope through a lumped-element high-pass filter. While this arrangement is sufficiently fast to easily resolve the beam's envelope, it was unable to resolve the beam's structure on time scales comparable to the RF period. However, with the filter removed, the diode left unbiased, and when connected directly into IAC's Tektronix DPO 71604 16 GHz oscilloscope, beam modulation at the RF scale could be resolved. And while that arrangement was still too slow to completely measure the shape of individual micropulses, it did enable extraction of the first six RF harmonics carried on the beam (2856, 5712, 8568, 11424, 14280, and 17136 MHz) using the oscilloscope's Fast Fourier Transform (FFT) capability. Reporting of the amplitudes of these harmonics will be our primary means of presenting our experimental data in this paper.

The second technique used was a short section of S-band WR 284 waveguide, equipped with a weakly-resonant cavity at one end, separated from the rest of the waveguide by an adjustable-width iris (Figs. 2 and 3).[22] In the testing reported here, the iris was set to provide a quality factor (Q) of approximately 60. At the opposite end of the waveguide from the cavity was a waveguide-to-coax transition, and for this work, the waveguide was directly connected through that transition via attenuators to the 16 GHz scope, with the measurements taken as described above. In testing, the waveguide was aligned to place the nominal beam axis perpendicular to the waveguide's long side, with the beam axis

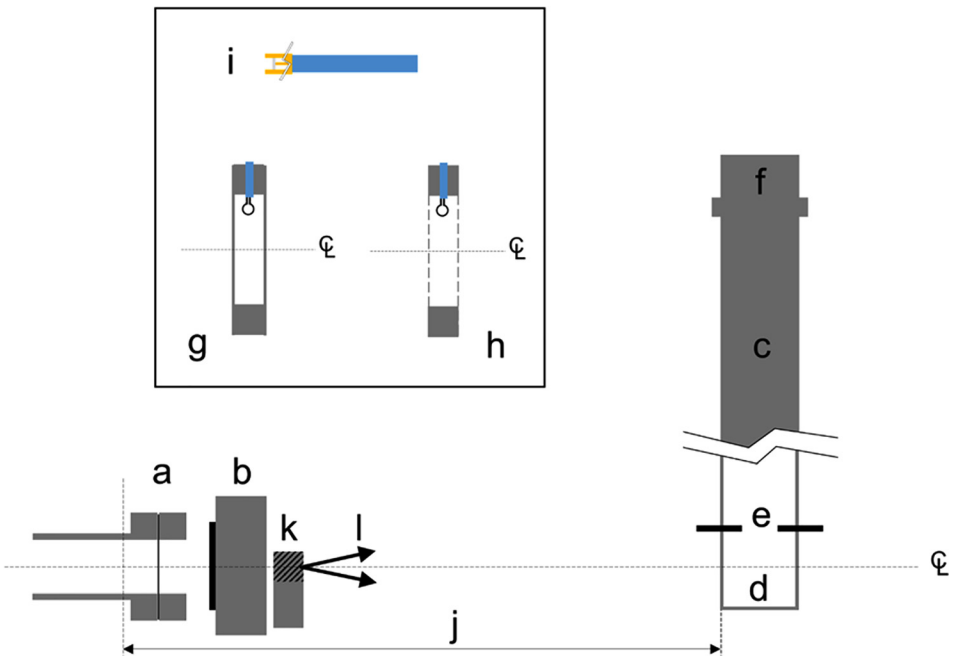

FIG. 2. Schematic of test configurations discussed in this paper (not to scale): (a) beam pipe and 0.254 cm Ti foil beam window; (b) x-ray converter; (c) S-band waveguide featuring interaction region (d) defined by variable iris (e) and terminating in a waveguide-to-coax transition (f); S-band pillbox cavity using $\dot{B}$ pickup with end plates installed (g) and with end plates removed (h) (analogous to the top left and top right panels in Fig. 3, respectively); diamond diode detector incorporated into SMA female connector (i). Distances downstream (j) are measured with respect to a reference location slightly upstream of the beam window shown in (a). During some testing, a 0.1 T permanent magnet (k) was added, intended to deflect secondary electrons to the right or left of the nominal beam path (l).

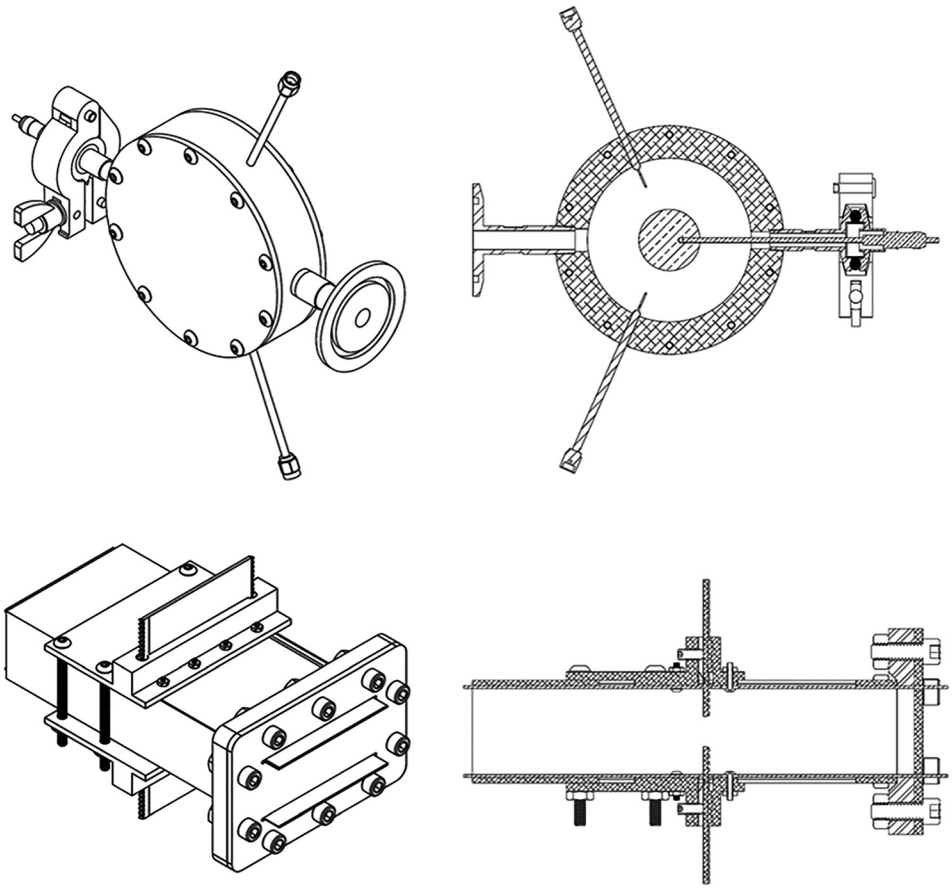

FIG. 3. External and cross-sectional diagrams of the S-band cavity (top) and S-band waveguide variable-geometry interaction region (bottom). The S-band cavity diagram shows two antennas, while only a single pickup loop was used in the actual experiment. Also, the cavity is shown with a charge-collection plate installed; this was not used in the tests reported here (From Ref. 22).

located 1/4 wavelength (at 2856 MHz) away from the cavity end to optimize generation of microwaves in the waveguide from the passage of the primary electron beam. Because the waveguide will support the 2856 MHz frequency and its higher harmonics, any such content present on the beam can generate microwave signals in the waveguide. In order for microwaves to be generated by x-rays passing through the waveguide, those x-rays must generate secondary electrons inside the waveguide, and this in turn requires that the secondary electrons (and therefore the incident x-rays) must be modulated at an RF frequency the waveguide can support.

The third and fourth techniques used an S-band pillbox cavity, previously described in detail in Ref. 22, equipped with a pickup ($\dot{B}$) loop to detect the azimuthal magnetic field and was tuned to 2854 MHz with a Q of 248 (Figs. 2 and 3). The cavity was also used with the end plates removed, spoiling the cavity resonance but allowing the $\dot{B}$ loop to directly sense the beam field alone (Figs. 2 and 4).

Note that each of these techniques is slightly different and therefore will have different responses to irradiation. The unbiased diamond diode detector is sensitive to the charge deposited on it. It and the $\dot{B}$ loop, which detects both the azimuthal magnetic field and whatever charge is directly deposited on it, are the most direct measurements of the beam. The outputs from the S-band cavity and waveguide are not primarily from the beam itself, but rather from microwave signals generated inside those structures by the passage of the primary electron beam, or by the secondary electrons generated by passage of the x-ray beam. As the cavity is only resonant at the fundamental frequency of 2856 MHz, all other frequency content introduced by the beam is suppressed relative to the fundamental. The S-band waveguide, however, is able to support not only the 2856 MHz fundamental but also its higher harmonics.

A motor-driven positioning system running on a pair of steel rails in an aluminum frame was used to adjust the location of these four detection systems, aligned to the nominal beam path by use of a visible alignment laser and measured with respect to a reference point on the beamline, just slightly upstream of the beam window (Fig. 2).

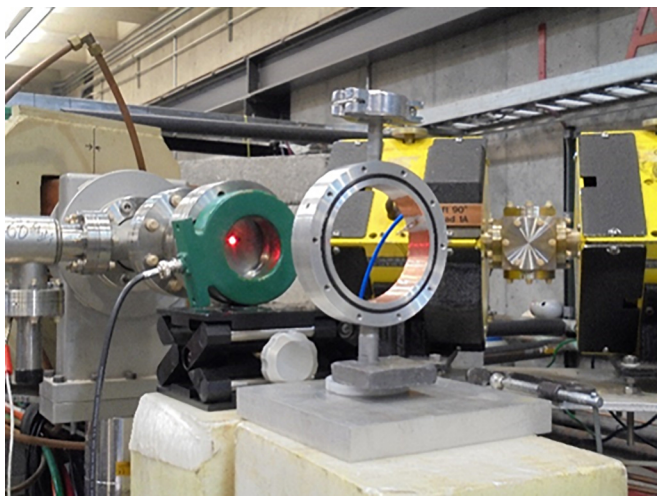

FIG. 4. S-band cavity installed on beam line, with end walls removed (from Ref. 22).

III. ELECTRON BEAM PROPAGATION IN AIR

Measurements were taken of the electron beam propagating in air using all four of the techniques discussed above. In each case, the device was connected directly to the 16 GHz scope (in some cases via attenuators), which was sufficiently fast to partially resolve the longitudinal structure of the electron beam signal. Two types of measurements of that signal were taken. First, the oscilloscope was used to perform a Fast Fourier Transform (FFT) of the signal, extracting the magnitudes of the harmonic components of the beam signal. With the diode detector, under ideal conditions, the fundamental and the next five higher harmonics could be detected, while in other cases fewer of the higher harmonics could be detected. The intensity of the FFT peaks, particularly for the higher harmonics, was sometimes too small to identify above the background. The relative strengths of the harmonics are reported in dB, although the oscilloscope settings and attenuators used differed for the different measurements, and therefore cannot provide quantitative comparisons of harmonic strengths between different measurements. The second measurement type is the peak-to-peak voltage of the beam-induced signal detected at the oscilloscope.

A. Diode

Two sets of measurements of the electron beam were taken with the diamond diode. The results of the first, low-spatial-resolution scan are shown in Fig. 5. This figure shows the signal strengths of the six harmonics measured as a function of distance. In this particular data set, the error in the measurement was estimated to be +/− 0.75 dB, and the noise floor was at approximately 63 dB. Although the 17136 MHz harmonic is nominally above the 16 GHz cutoff of the oscilloscope, it was very clearly identifiable during this measurement.

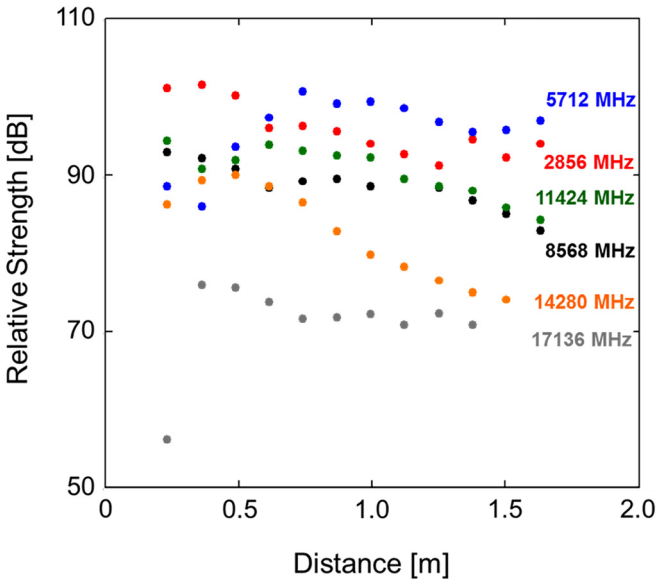

FIG. 5. Relative strength of the first six harmonics of the electron beam signal detected with the diamond diode, as a function of distance, during the initial measurement.

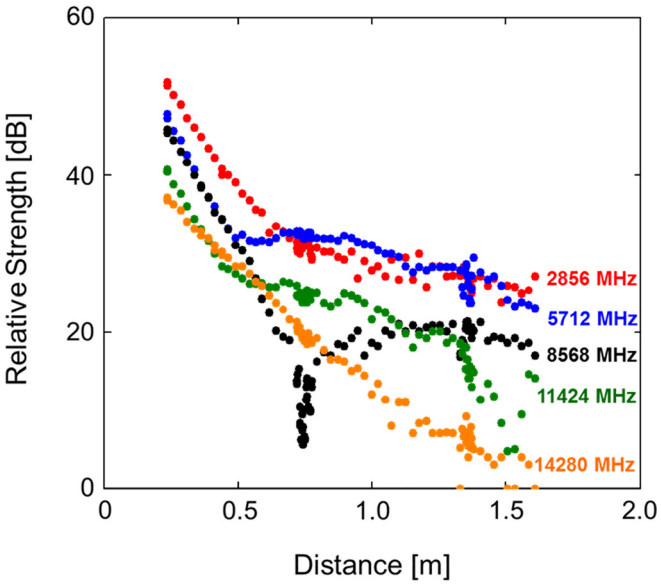

FIG. 6. Relative strength of the first five harmonics of the electron beam signal detected with the diamond diode, as a function of distance.

The second set of measurements was intended to provide increased spatial resolution, and the results are shown in Figs. 6 and 7. Figure 6 shows the relative strengths of the first five harmonics of the RF frequency detected by FFT of the electron beam signal on the diamond diode, as a function of distance. For the first 50 cm, there is a steady decline in the strength of all the harmonics. At 50 cm, the 5712 MHz signal goes through a minimum and increases slightly before decreasing at a reduced slope, while the fundamental and 11424 MHz component go through inflections, and the 8568 MHz harmonic reaches a sharp minimum at 74 cm. After this location, the declines in the first four harmonics are generally slower, while the fifth harmonic's decrease is largely unchanged. Additional minima are present, most noticeably in the fourth harmonic at 84, 115, and 151 cm. No significant minima or nulls are present in the fundamental.

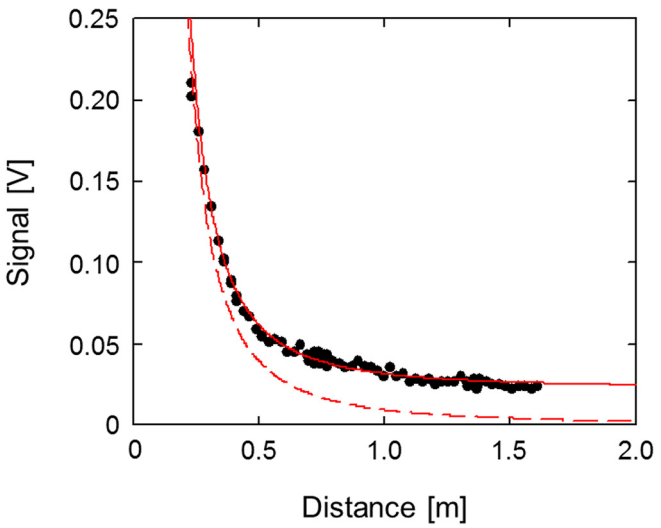

FIG. 7. Peak-to-peak signal measured with diode (points) compared to signal calculated from beam density with (solid red) and without (dashed red) background signal.

Comparing the low-resolution scan of Fig. 5 and the high-resolution scan of Fig. 6 is somewhat difficult. In both cases, the strength of the 2856 MHz fundamental is higher than that of the 5712 MHz harmonic until approximately 60 cm, after which the latter is generally stronger. The 5712 MHz harmonics go through minima prior to this point in each data set, but that location is at 36 cm in the low-resolution data and 57 cm in the high resolution data. The pronounced minimum in the 8568 MHz harmonic at 74 cm in the high resolution data is missing in the low-resolution data, which exhibits a weak minimum at 61 cm. Similarly, the strong minimum at 151 cm in the 11424 MHz harmonic in the high resolution scan is absent in the low resolution data. The different spatial resolution of the two scans by itself does not appear to explain these differences, as several data points in the low resolution scan were taken at locations that fell inside the wide minima seen in the higher harmonics in the high resolution scan. These two measurements were taken on different days, and although the accelerator and test configurations were believed to be identical, the most likely explanation for these differences lies in an unnoticed change in the system. Different oscilloscope settings were used in the two measurements, so the magnitudes of the harmonic components differ.

The peak-to-peak signal amplitude measured with the diode during the high-spatial-resolution scan, as a function of diode position, is shown in Fig. 7. This data does not exactly follow the expected inverse square law relation. From the measured beam envelope shown in Fig. 1, we have already inferred an approximate beam envelope $w(z)$, given in Eq. (1). This implies a beam current density of

$$J(z) = (0.095\text{A})/\pi w(z)^2. \tag{2}$$

In normal operation, the diamond element is biased with a potential of 150 V to extract free charge carriers liberated by incident radiation. However, we are using it in unbiased mode, and it is therefore likely that the diamond element itself is inert, but the female SMA connector in which it is housed is acting as a charge collector (or an emitter, depending on its secondary electron yield). Assuming a charge interception area defined by an inner diameter of 2.54 mm, multiplying Eq. (2) by this area, and multiplying this computed current by 50 Ω yields the predicted signal voltage amplitude as a function of distance. This is represented by the dashed red curve in Fig. 7 and is clearly insufficient to explain the data. However, when we assume an additional, constant background equivalent to 22 A/m^2, this generates the solid red curve, which provides reasonable agreement to the data. It is important to note that the range of the beam electrons in the detector is much longer than the size of the detector, so a complete analysis would need to incorporate secondary electron generation from the detector. Also, remember that the signal strength plotted here is the peak-to-peak voltage measured at the oscilloscope. Any noise or DC offset would not have affected the peak-to-peak voltage in this way. Instead, the "background" signal must have the same pulse structure and arrive with the same phase as the electron beam pulse train. It is possible that this is due to additional x-ray radiation present in the environment, which is produced with the same pulse structure as the primary electron beam. Indeed, with the diode placed close to the beam line but away from the beam window, a small background signal, assumed to be due to x-rays, could be detected which retained the harmonic content of the primary electron beam itself. This signal disappeared when the line of sight between the diode and the beam line was blocked by a lead brick or moved below the heavy metal table on which the experiment was mounted. Note that the data transitions from being dominated by the inverse square law (presumably due to primary electrons) to the background level (possibly due to x-rays) at approximately 0.5 m, which is also the onset of the significant changes in the harmonic content shown in Fig. 6 and discussed above. At this location, Eq. (1) shows that the beam half-width is less than 3 cm, and therefore has not expanded to the point where it could strike the track or table on which the experiment was mounted and generate additional background radiation in the process. No nulls are apparent in the peak-to-peak signal voltage shown in Fig. 7.

B. $\dot{B}$ loop

Measurements of the electron beam taken with the $\dot{B}$ loop (the S-band cavity with end plates removed, as in Fig. 4) are shown in Fig. 8. The strengths of the harmonics decrease smoothly with increasing distance, with the only major null occurring in the 11424 MHz signal near 1.13m and a weaker null in the 14280 MHz signal at 139 cm. Note that the relative strengths of the harmonics do not appear to change significantly in this case.

C. Cavity

Measurements of the signal induced in the S-band cavity under electron bombardment, as a function of position, are shown in Figs. 9 and 10. The peak-to-peak signal strength and the fundamental are very strong, and so a 5x attenuator

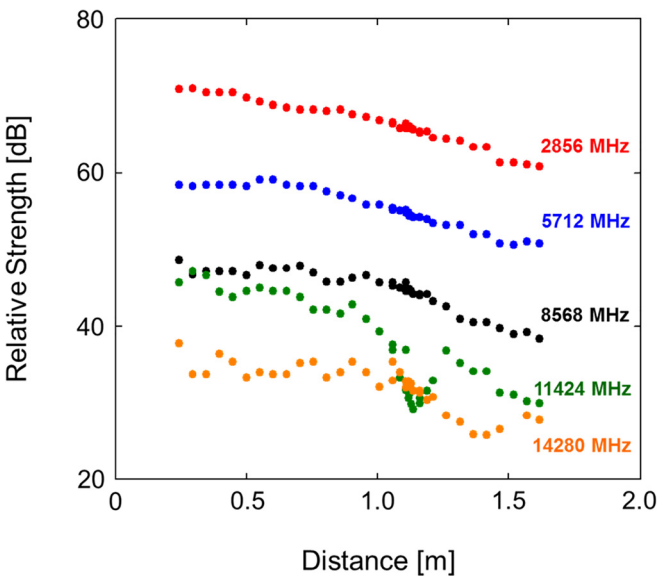

FIG. 8. Relative strength of the first five harmonics of the electron beam signal detected with the $\dot{B}$ loop, as a function of distance.

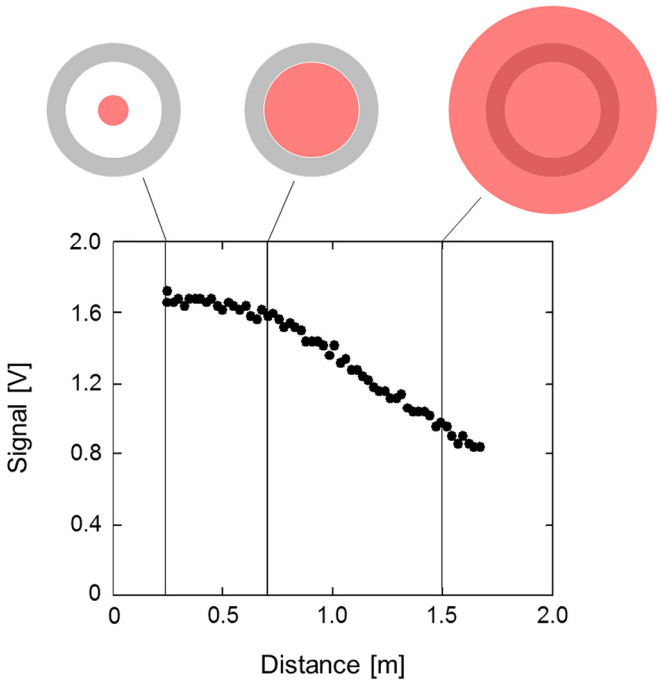

FIG. 9. Peak-to-peak signal measured with cavity. Images at top compare the size of the cavity body (gray) with the beam size (red), using the fit for beam half width in Eq. (1).

was installed during these measurements. No significant harmonic content was seen except at the fundamental, as the cavity is not resonant at the higher harmonics. Although the cavity can't support these modes, they are still present in the beam, and the $\dot{B}$ loop will detect them, and so the difference in the response of the cavity at the fundamental and higher harmonics is a measure of the relative strengths of resonant and non-resonant beam-cavity interactions. No clear nulls are present. A clear change in the slope of the signal strength occurs when the beam half-width equals the cavity inner radius of 4 cm (Fig. 9). At distances closer than this, the beam under-fills the cavity, so all of its current aids in driving the cavity mode, while at distances larger than this, the beam over-fills the cavity, so that increasingly large amounts of the beam do not participate in driving the cavity mode.

D. Waveguide

The response of the S-band waveguide to the electron beam is shown in Fig. 11. The interaction region iris had been adjusted to provide a broad resonance at 2856 MHz, which was 10s of MHz wide, and a 20 dB attenuator was used between the waveguide and the oscilloscope. No nulls are present in the data. As discussed previously, this is not a direct measurement of the beam harmonic content, but rather a measurement of the frequency content of the microwaves generated inside the waveguide by the passage of the electron beam, and by the secondary electrons generated inside the waveguide by the primary electron beam. As such there is a difference in the spectrum indicated compared to more direct measurements using the diamond diode and the $\dot{B}$ loop. For example, in both this case and in part of the S-band cavity measurements, the 11424 MHz signal is stronger than the 5712 MHz signal. However, there does again appear to be a change in the shape of the data sets occurring around 50 cm – 60 cm downstream, as seen in the S-band cavity measurements, in this case taking the form of an increase in the steepness of the curves for the 2856, 11424, and 5712 MHz harmonics, and a disappearance of the 8568 and 14280 MHz harmonics. Again, the effect is likely geometric. To optimize the S-band interaction, the nominal beam center was aligned to the waveguide interaction region center, which was located a quarter wavelength (2.6 cm) from the end of the waveguide. Equation (1) shows that the beam radius should be equal to 2.6 cm at a location of 47 cm downstream. Beyond this point, the entire beam will no longer strike the waveguide. Additionally, the inside half-height of WR 284 waveguide is 3.6 cm, which Eq. (1) shows will equal the beam radius at a location of 64 cm downstream.

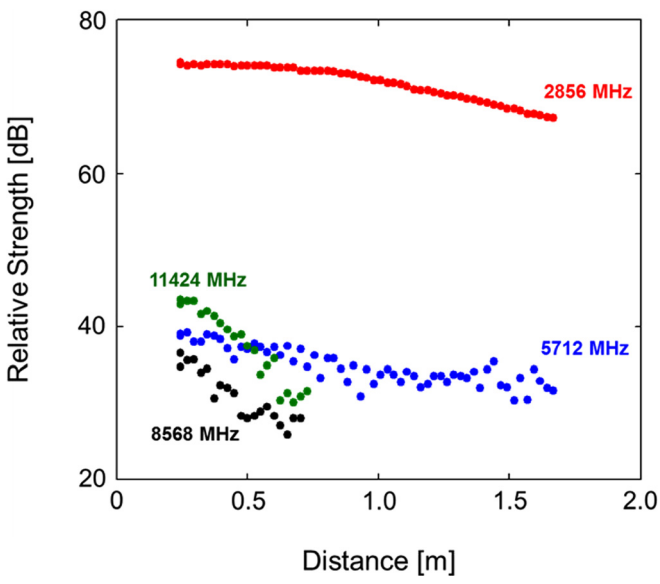

FIG. 10. Relative strength of the first four harmonics of the electron beam signal detected with the S-band cavity, as a function of distance.

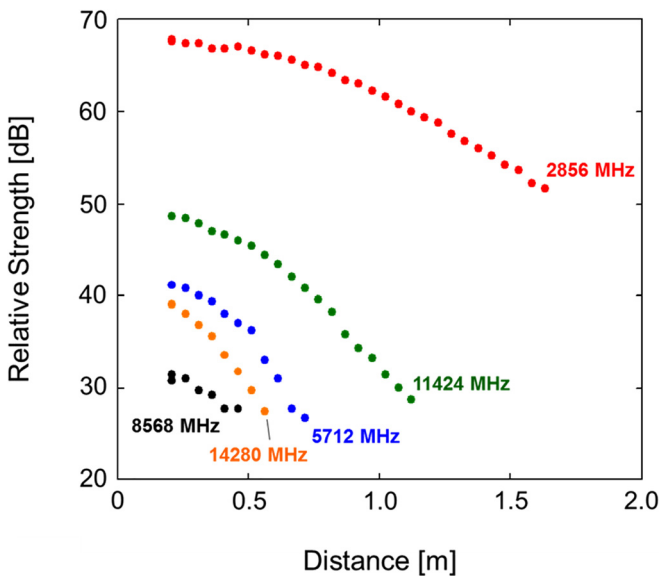

FIG. 11. Relative strength of the first five harmonics of the electron beam RF frequency detected with the waveguide, as a function of distance.

Beyond this point, increases in beam radius will increase the fraction of the beam passing over and under the waveguide, as well as past its end, reducing the interaction efficiency.

IV. X-RAY CONVERTER

For these measurements, the x-ray converter was installed downstream of the beam window as shown in Fig. 2.

A. Diode

Measurements were performed using the diode to measure the x-ray signal as a function of distance in air. The measureable signal strength with the x-ray beam was significantly less than with the electron beam, and the signal could only be detected over a much shorter distance. Additionally, not all higher harmonics could be detected above the noise floor on every shot. The results are shown in Fig. 12.

As with the earlier diode measurements, a preliminary low-spatial-resolution scan was initially taken. This occurred on a different day than the data presented in Fig. 12 and seemed to exhibit some differences from the higher resolution scans shown here, but no definitive statements could be made due to the low resolution. If these differences were present, they would indicate changes in the system response that were due to variables that were being insufficiently controlled, and this is consistent with hints present in other testing with the diode. Potential issues with the diode in this connection include angular misorientation of the diode and changes in the locations, and therefore the radiation induced currents, in the diode cables.

B. Waveguide

Measurements of the waveguide response to the x-ray beam as a function of position are shown in Figs. 13–15. The strength of the 2856 MHz and its integer harmonic microwave signals induced in the waveguide are shown in Fig. 13. These signals clearly exhibit very strong nulls as the location of the waveguide is changed, which were found to be highly reproducible. The top graph in Fig. 14 shows the fundamental strength as a function of waveguide location, isolated from the higher harmonics for clarity, and the top panel in Fig. 15 shows the peak-to-peak signal strength. The noise level in the latter graph was 5 mV, or approximately the size of the individual points in the graph.

Again we note that, because of the design of the x-ray converter, primary electrons are blocked from reaching the waveguide. The microwave signals generated in the waveguide are therefore induced by the passage of x-rays through the waveguide, generating secondary electrons inside the waveguide which generated these microwave signals. The

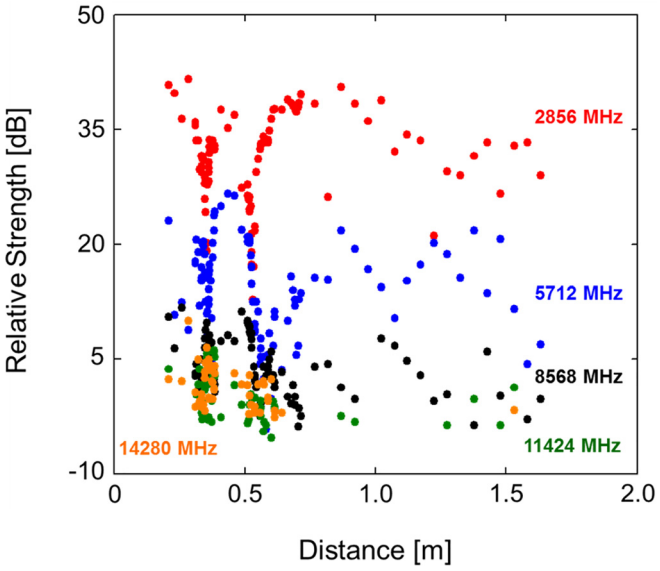

FIG. 13. Relative strength of the first five harmonics of the x-ray beam signal detected with the waveguide, as a function of distance.

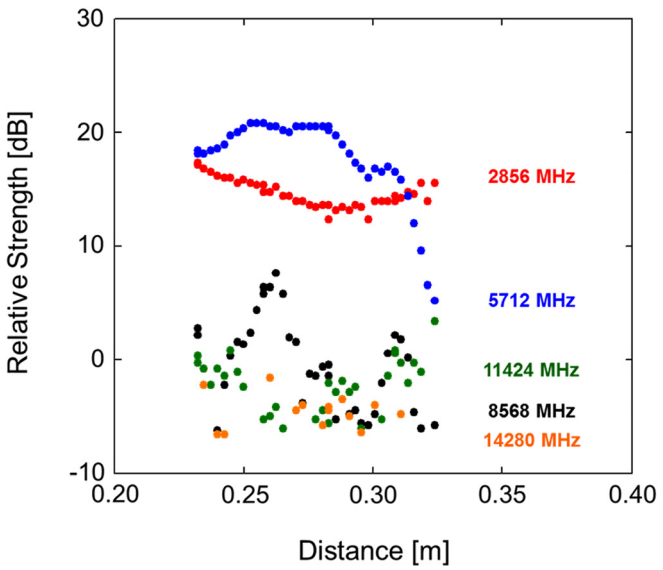

FIG. 12. Relative strength of the first four harmonics of the x-ray beam signal detected with the diamond diode, as a function of distance, second data set.

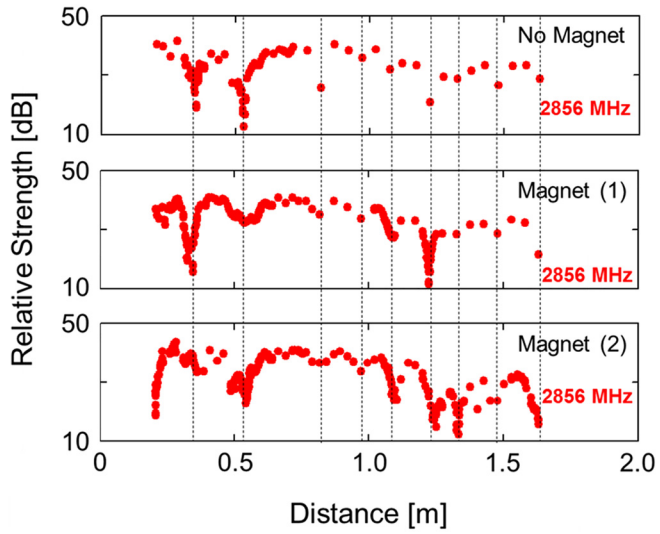

FIG. 14. Relative strength of the 2856 MHz harmonics of the x-ray beam signal detected with the waveguide, as a function of distance, without the magnet installed (top) and with the magnet installed in two different orientations (center, bottom).

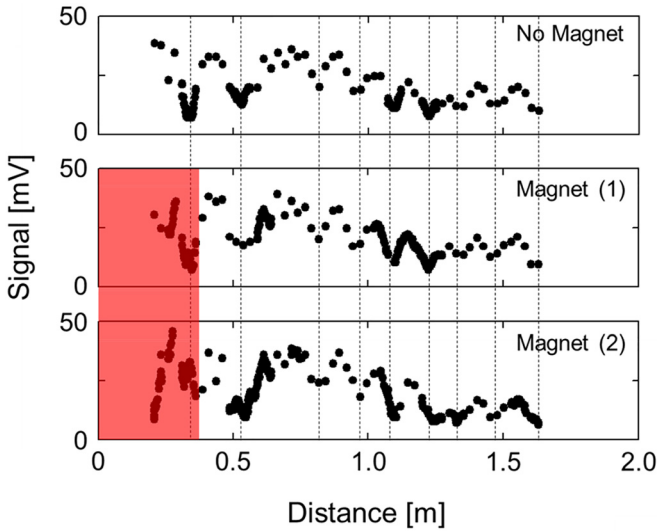

FIG. 15. Peak-to-peak signal measured with the waveguide, with the x-ray converter installed, as a function of distance, without a magnet (top), and with the magnet installed in two different polarities (center, bottom). The vertical lines indicating the presence of nulls are in the same locations here as in Fig. 14, demonstrating that nulls in the total signal coincide with nulls in the fundamental.

presence of not only the 2856 MHz signal but also the higher harmonics suggests that the RF modulation present in the primary electron beam is imprinted onto the x-rays generated in the x-ray converter and is then imprinted onto the secondary electrons produced by the modulated x-rays in the waveguide. This is consistent with our previous observations in Ref. 22. The passage of the modulated x-rays through the x-ray converter will also presumably liberate RF-modulated secondary electrons from the downstream face of the x-ray converter; this will be discussed in more detail below.

V. ALUMINUM PLATES

A limited number of shots were also taken using the unpowered diode as a detector, and replacing the x-ray converter with between 0.318 cm and 2.54 cm of aluminum, varying in 0.318 cm increments. This data was taken over two days. Although some signal nulls were seen, the location and depth of these nulls in the fundamental on the first day were not seen to vary substantially as a function of aluminum thickness. However, the location and depth of the nulls did vary from the first day to the second day. The test configuration was nominally the same on both days, and this again implies the presence of subtle changes, most likely associated with the diode configuration. Only a single thickness of aluminum was used on the second day, 0.635 cm, and those results will be discussed below.

VI. MAGNETIC FIELD EFFECT ON SECONDARY ELECTRONS

The presence of the nulls in the signals observed under various test configurations was unexpected. One possibility was that secondary electrons produced by the passage of the primary electron beam through the Ti foil beam window or Al plates, or by the passage of x-rays through the Al plates or x-ray converter, might play a role. The interaction of x-rays with the cavity and waveguide, for example, indicates that secondary electrons produced by the passage of the RF-modulated x-rays generated secondary electrons carrying the same RF modulation. These secondary electrons would be traveling at a variety of velocities, all of which are slower than the primary electrons or the x-rays, leading to locations downstream where their modulation would be in phase or out of phase with each other and with that of the primary electrons or x-rays, generating an interference-like effect. To assess this, a permanent magnet with peak field of 0.107 T, 2.54 cm square cross section, and 2.54 cm gap, was placed immediately downstream of the aluminum plates and x-ray converter, in order to deflect any secondary electrons (Fig. 2). The magnetic field as a function of position, indexed to the upstream face of the magnet, is shown in Fig. 16. The upstream face of the magnet was flush with the downstream face of the x-ray converter or Al plates; with the x-ray converter in place, this plane was 11.7 cm downstream from the reference plane. If the magnetic field B_o acts over an effective length d, then the deflection angle θ is given by

$$\sin\theta = \mathrm{B_o}d\,(1.7\times10^{-3}\beta_s\gamma_s)^{-1} \tag{3}$$

with $B_o d$ in units of Tesla-meters and where β_s and γ_s are the relativistic parameters. For a field strength of 0.1 T, and an effective distance of 2.54 cm, we have

$$\sin\theta = 1.47/(\beta_s\gamma_s). \tag{4}$$

Simulations of secondary electron generation from the x-ray converter were performed using the radiation transport code Monte Carlo N-Particle, Version 6.1.1 (MCNP6).[32] The measured beam profile for the 2856 MHz linear accelerator and the x-ray converter dimensions was simulated in MCNP6. The energy spectrum of secondary electrons generated from the converter was tallied over a logarithmically spaced energy bin structure. The simulation results are

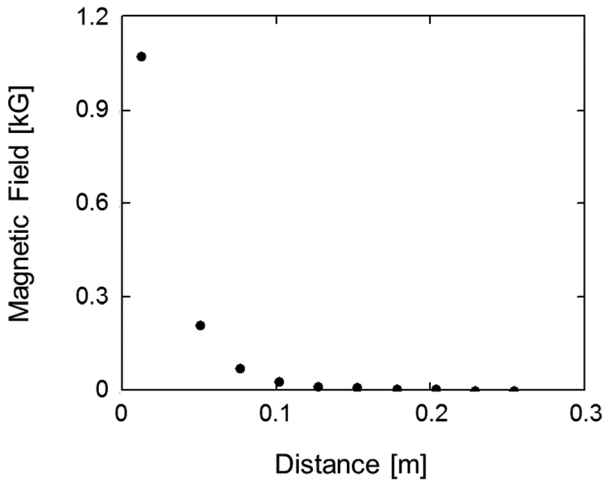

FIG. 16. Magnetic field as a function of position, measured relative to the upstream edge of the magnet. Note that these distances are offset from those used in other figures.

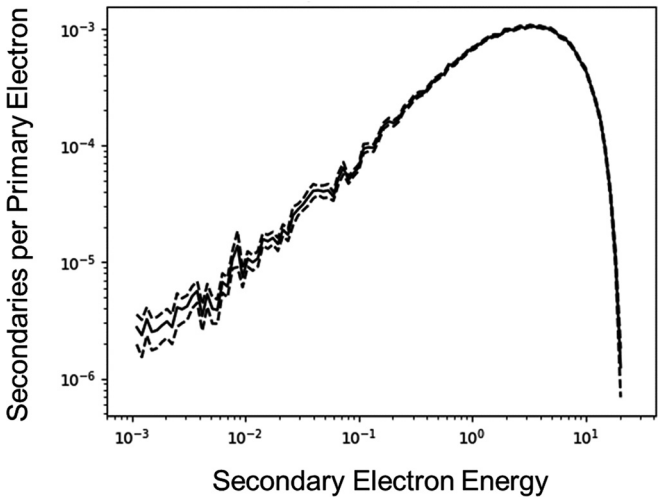

FIG. 17. Secondary electron spectral profile exiting x-ray converter, as simulated using MCNP6.

shown in Fig. 17 for the distribution of secondary electrons exiting the converter per primary source electron. The solid line is the statistical mean and the dashed lines show the statistical confidence range of two standard deviations (95% confidence). The results show that the peak secondary electron energy is approximately 3 MeV, which per Eq. (4) implies a deflection of about 12.5° by the magnet. To experimentally assess the effect of this magnetic field on the system response, three test configurations were used: (1) x-ray converter with diode detector, (2) Al plate stack with diode detector, and (3) x-ray converter with waveguide detector.

A. X-ray converter with diode detector

Figure 18 shows the 2856 MHz fundamental and next two higher harmonics detected by the diode as a function of distance, with and without the magnet; the data without the magnet are repeated from Fig. 12. Due to the small size of the diode and its placement on the nominal beam axis, only a single polarity of the magnetic field was used. The results with and without the magnet are essentially identical.

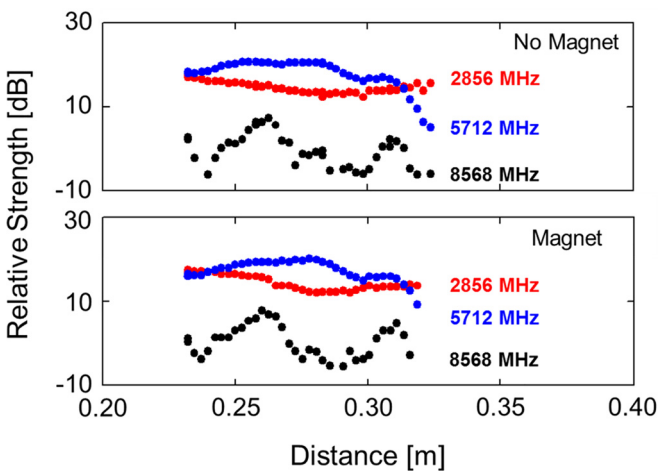

FIG. 18. Relative strength of the first three harmonics of the x-ray beam signal detected with the diode, as a function of distance, without the magnet installed (top) and with the magnet installed (bottom).

B. Al plate stack with diode detector

Figure 19 shows the relative strength of the 2856 MHz fundamental detected with the diode, as a function of diode location, with 0.635 cm of Al used in lieu of the x-ray converter, with and without the magnet. Again, a single magnet orientation was used. The results in the two cases were essentially unchanged for distances greater than 32 cm; this corresponds well to the location of 33 cm at which the magnetic field has fallen to 1 G.[33] At distances closer than this, the magnetic field extends into the diode and could affect the trajectories of any secondary electrons produced inside or outside it. Note that because the Al thickness used here was less than the CSDA range for 20 MeV electrons in Al (which is 3.91 cm), radiation reaching the diode likely consists of a combination of primary electrons and x-rays.

C. X-ray converter and waveguide

The relative strength of the 2856 MHz fundamental and the peak-to-peak signal strength, as a function of waveguide location with the x-ray converter installed, are shown in Figs. 14 and 15. Each figure shows the results without the magnet (as discussed previously) and with the magnet in two different orientations; the magnetic field orientation was changed by flipping the magnet in such a way that its mass shielding contribution would be unchanged. Because the waveguide's interaction region, defined by the variable iris, was aligned to the nominal beam path with the alignment laser, the bulk of the waveguide is to the left of the nominal beam path when facing downstream (Fig. 2). Thus, if secondary electrons produced at the downstream face of the x-ray converter were affecting the pattern of measured nulls, we would also expect an asymmetry in response depending on whether the secondaries were deflected to the left or to the right. In particular, with the magnet deflecting the secondaries to the right, they would only need to be deflected by a few centimeters to entirely miss the waveguide; taking

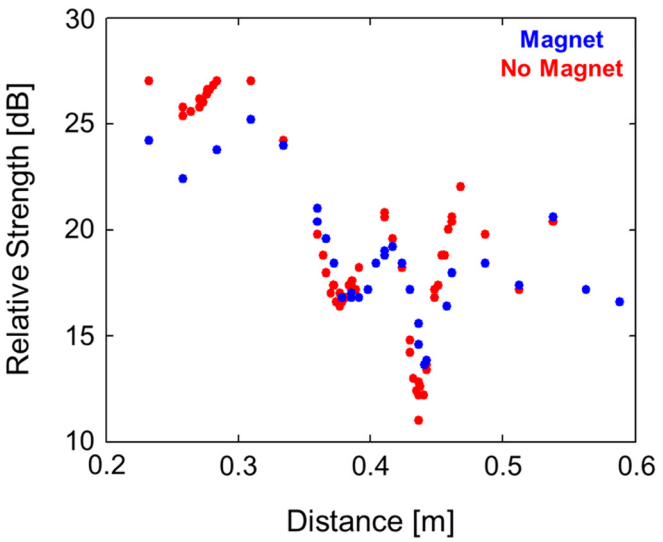

FIG. 19. 2856 MHz fundamental detected with the diode detector, as a function of detector position, with 2/8″ Al installed in lieu of x-ray converter, with and without magnet.

5 cm to be conservative, this means that the secondaries from the front face of the x-ray converter would miss the waveguide once it was approximately 23 cm downstream from the x-ray converter, or at a location $z = 34.7$ cm downstream from the reference plane. With the magnet deflecting the secondaries to the left, they would have to be deflected by 36.8 cm to miss the waveguide, which would happen when the waveguide was approximately 166 cm downstream from the x-ray converter, or at a location of $z = 178$ m downstream from the reference plane, a longer distance than was available in this testing. This implies that if secondaries play a role, a difference in the waveguide response under the two field configurations should be found in the region from 34.7 cm to 178 cm.

However, no substantial change in waveguide response was found due to the presence or polarity of the magnetic field at distances greater than approximately 37 cm. These results, like those above, are not consistent with the hypothesis that secondary electrons produced from the downstream face of the x-ray converter play any significant role in determining the system response. First, there was very little change at longer distances, where the magnetic deflection of the secondaries through a particular angle should have been most effective in preventing them from striking the waveguide. Second, there was no significant asymmetry between the case where the secondaries were being deflected to the left and into the waveguide body, and the case where the secondaries were being deflected to the right and past the waveguide body.

However, secondary electrons also play a role *inside* the waveguide, and so we may ask whether the differences seen at locations closer than 37 cm are due to the magnet penetrating into the waveguide and altering the trajectories, and therefore the microwave fields generated by, the x-ray-induced secondary electrons there. The inside dimensions of WR 284 waveguide are approximately 72 mm x 34 mm. In order for an external magnetic field to *not* significantly perturb the x-ray-generated secondary electrons inside the waveguide, the resulting cyclotron radius should be larger than the waveguide dimensions. At an applied field of 1 G, which is roughly twice the Earth's field, this will happen for any secondary electron with an energy of 4.5 eV or higher. The field from the magnet reaches 1 G at 25.4 cm downstream from its upstream face, or at a distance $z = 37.1$ cm downstream from the reference plane, and so at distances larger than this we can assume that the magnetic field effect on secondaries inside the waveguide is negligible. This region is indicated with red shading in Fig. 15 and clearly encompasses the entire region of significant differences between the three cases. Thus, it seems likely that deflection of x-ray-induced secondary electrons inside the waveguide is the source of the different behavior seen in Figs. 14 and 15.

Finally, note that the top two graphs in Figs. 14 and 15 were taken on one day, while the bottom graph in each figure was taken on the following day. In contrast to the diode data, which seemed to exhibit day-to-day variations in the locations of nulls, the nulls indicated in these figures, downstream of the region of magnetic influence, appear remarkably similar.

VII. DISCUSSION

Here we reported a direct measurement of the RF fundamental and higher harmonics in electron and x-ray beams propagating in air. Measurements were also made of the RF content of the signals generated in a waveguide by passage of electrons and x-rays through it. These signals must be produced by secondary electrons generated inside the waveguide, and their measurement supports our conclusions from Ref. 22 that the RF modulation of the primary electron beam is impressed onto the x-ray signal and is still present in the secondary electrons generated by those x-rays

Four techniques were used for measuring the electron beam: unbiased diamond diode, S-band cavity, $\dot{B}$ loop, and S-band waveguide, while measurements of the x-ray beam were taken with the diode and the waveguide. The responses of these techniques differed. The $\dot{B}$ loop is likely to be the best measurement of electron beam frequency content. In particular, close to the beam window where the beam is small, this is the only non-intercepting technique used here, and as such it avoids secondary electron formation which can complicate interpreting data. Also, unlike the cavity and waveguide, it is not resonant and therefore will not serve to select or suppress certain frequencies.

The cavity and waveguide both exhibited some frequency-selective behavior. In the cavity, which was only resonant at 2856 MHz, the response to the higher harmonics was much weaker, and in both the cavity and the waveguide, the relative strengths of the higher harmonics did not decrease with increasing frequency, but instead appeared "out of order."

Throughout the experiments, there were local minima or nulls in the system response. Under electron beam irradiation, these occurred only in the higher harmonics measured with the diode and $\dot{B}$ loop, while under x-ray irradiation more variations occurred with the diamond diode, and very strong, quasiperiodic nulls occurred in the waveguide response.

Comparison of preliminary low resolution and final high resolution measurements taken with the diode suggested sensitivity of the system response to minor changes in parameters such as diode orientation or cable locations. Such day-to-day variations were not present on the waveguide measurements.

The null behavior, particularly in the waveguide, is suggestive of an interference phenomenon. Interference of the x-ray signals themselves can be ruled out. However, the waveguide introduces several opportunities for interference between microwave signals generated by the passage of the x-ray beam. The waveguide is larger than the 10.5 cm wavelength of the 2856 MHz fundamental. If the modulated x-ray signal arrives at different locations along the waveguide with slightly different phases, it will generate secondary electrons inside the waveguide, which in turn will generate electromagnetic radiation propagating in both directions along the waveguide. One of these signals will travel directly to the waveguide to coax transition, while the other will travel to the shorted end of the waveguide and be reflected back towards the transition, where the two signals can add constructively or

destructively depending on their relative phase, which depends in turn on where they were created. Thus, the irradiation of the waveguide provides for a distributed source of microwaves, created with slightly different phases depending on location, and generating two signals which can recombine to interfere with each other. Varying the location of the waveguide changes the relative phases of the source terms. This may help to explain, at least qualitatively, the behavior of the waveguide.

A potential additional factor was the generation of secondary electrons from the x-ray converter. These electrons will be generated with the RF modulation of the x-rays, but would travel more slowly, causing their contributions to detector response to vary periodically with position. However, we were able to rule out any significant contributions to the effect by these secondaries by using a magnet to deflect them away from the nominal beam path. The presence of this magnet had no significant effect on the system frequency response at long distances, where the removal of secondaries should have been most effective. The only significant changes occurred when the detectors were so close to the magnet that the magnetic field penetrated into them. This change was particularly evident in the waveguide measurements, suggesting that the magnet was altering the trajectories, and therefore the microwave generation, of the secondary electrons created inside the waveguide by the x-ray signal.

ACKNOWLEDGMENTS

The authors gratefully acknowledge the superb support provided by the team at the Idaho Accelerator Center, and in particular, J. Stoner, C. O'Neill, and K. Folkman, without whom this work would not have been possible.

[1]J. R. Harris and P. G. O'Shea, IEEE Trans. Electron Devices **53**, 2824–2829 (2006).
[2]J. G. Neumann, J. R. Harris, B. Quinn, and P. G. O'Shea, Rev. Sci. Instrum. **76**, 033303 (2005).
[3]K. R. Spangenberg, *Vacuum Tubes* (McGraw-Hill, New York, 1948).
[4]C. A. Spindt, C. E. Holland, A. Rosengreen, and I. Brodie, IEEE Trans. Electron Devices **38**, 2355 (1991).
[5]A. Pedersen, A. Manolescu, and A. Valfells, Phys. Rev. Lett. **104**, 175002 (2010).
[6]K. L. Jensen, D. A. Shiffler, I. M. Rittersdorf, J. L. Lebowitz, J. R. Harris, Y. Y. Lau, J. J. Petillo, W. Tang, and J. W. Luginsland, J. Appl. Phys. **117**, 194902 (2015).
[7]M. Reiser, *Theory and Design of Charged Particle Beams* (Wiley, New York, 1994).
[8]R. B. Miller, *An Introduction to the Physics of Intense Charged Particle Beams* (Plenum Press, New York, 1982).
[9]P. G. O'Shea, R. A. Kishek, M. Reiser, B. Beaudoin, S. Bernal, Y. Cui, A. Diep, D. Feldman, M. Glanzer, T. F. Godlove, I. Haber, J. Harris, H. Li, J. Neumann, B. Quinn, M. Qurius, M. Snowel, A. Valfells, M. Virgo, M. Walter, R. Yun, and Y. Zou, Laser Part. Beams **20**, 599 (2002).
[10]S. Bernal, B. Beaudoin, Y. Cui, M. Glanzer, T. F. Godlove, J. Harris, M. Holloway, I. Haber, R. A. Kishek, W.-T. Lee, H. Li, D. Lamb, B. Quinn, M. Qurius, M. Reiser, A. Valfells, M. Walter, M. Wilson, R. Yun, Y. Zou, and P. G. O'Shea, Nucl. Instrum. Methods Phys. Res. A **519**, 380–387 (2004).
[11]A. Faltens, E. P. Lee, and S. S. Rosenblum, J. Appl. Phys. **61**, 5219 (1987).
[12]J. R. Harris, J. G. Neumann, K. Tian, and P. G. O'Shea, Phys. Rev. E **76**, 026402 (2007).
[13]J. R. Harris and P. G. O'Shea, Phys. Plasmas **15**, 123106 (2008).
[14]J. R. Harris and J. W. Lewellen, J. Appl. Phys. **108**, 083301 (2010).
[15]B. R. Poole and J. R. Harris, Phys. Plasmas **20**, 043108 (2013).
[16]A. Gover, Phys. Rev. Spec. Top.—Accel. Beams **8**, 030701 (2005).
[17]Y. C. Mo, R. A. Kishek, D. Feldman, I. Haber, B. Beaudoin, P. G. O'Shea, and J. C. T. Thangaraj, Phys. Rev. Lett. **110**, 084802 (2013).
[18]B. R. Poole, D. T. Blackfield, Y.-J. Chen, J. R. Harris, and P. G. O'Shea, "Space charge waves in mismatched beams," in *Proceedings of the 2009 Particle Accelerator Conference*, Vancouver, Canada, 4–8 May 2009.
[19]J. R. Harris, J. W. Lewellen, and B. R. Poole, J. Appl. Phys. **114**, 063304 (2013).
[20]J. R. Harris, J. W. Lewellen, and B. R. Poole, J. Appl. Phys. **116**, 133302 (2014).
[21]J. R. Harris, B. R. Poole, and J. W. Lewellen, J. Appl. Phys. **122**, 093302 (2017).
[22]J. R. Harris and R. B. Miller, J. Appl. Phys. **123**, 083302 (2018).
[23]R. B. Miller, U.S. patent 5,608,403 (March 4, 1997).
[24]K. C. Gendreau, Z. Arzoumanian, S. J. Kenyon, and N. S. Spartana, U.S. patent 9,117,622 (August 25, 2015).
[25]J. Mitchell, "Pulsar navigation & x-ray communication demonstrations with the NICER payload on ISS," in *1st Annual ISS R&D Conference*, Denver, CO, 25–28 June 2012.
[26]L. M. B. Winternitz, K. C. Gendreau, M. A. Hassouneh, J. W. Mitchell, W. H. Fong, W.-T. Lee, F. Gavriil, and Z. Arzoumanian, "The role of x-rays in future space navigation and communication," in *36th Annual AAS Guidance and Control Conference*, Breckenridge, CO, 1–6 February 2013.
[27]S. Li-zhi, Z. Bao-sheng, and L. Yong-an, "Advances in x-ray/EUV optics and components IX," Proc. SPIE **9207**, 920716 (2014).
[28]H. Li, X. Tang, S. Hang, Y. Liu, and D. Chen, J. Appl. Phys. **121**, 123101 (2017).
[29]S. Shi-Bin, X. Lu-Ping, Z. Hua, and G. Na, Chin. Phys. B **24**, 094215 (2015).
[30]See iac.isu.edu for more information about the Idaho Accelerator Center.
[31]See http://www.aasc.net/products/diamond-radiation-detectors for more information on this product.
[32]T. Goorley, "MCNP6.1.1-Beta Release Notes," Report No. LA-UR-14-24680, 2014.
[33]Figure 16 shows the magnetic field measured a locations relative to the magnet's upstream face. During these tests, the magnet's upstream face was 7.62 cm downstream of the reference location used for other distance measurements in this paper.